Supporting information for

Ultra-highly saturated structural colors enhanced by multipolar-modulated metasurfaces

Bo Yang, [†] *Wenwei Liu,* [†] *Zhancheng Li,* [†] *Hua Cheng,* [†] *Duk-Yong Choi,*[*, //, ⊥] *Shuqi Chen,* [*, †, ‡, §] *and Jianguo Tian* [†, ‡]

[†]The Key Laboratory of Weak Light Nonlinear Photonics, Ministry of Education, School of Physics and TEDA Institute of Applied Physics and [‡]Renewable Energy Conversion and Storage Center, Nankai University, Tianjin 300071, China

[§]The Collaborative Innovation Center of Extreme Optics, Shanxi University, Taiyuan, Shanxi 030006, China

[//] Laser Physics Centre, Research School of Physics and Engineering, Australian National University, Canberra, ACT 2601, Australia

[⊥]College of Information Science and Technology, Jinan University, Guangzhou 510632, China

**Corresponding author. Emails: duk.choi@anu.edu.au; schen@nankai.edu.cn*

This file includes:

S1 Multipolar decomposition for three primary colors

The reflection spectra and multipolar decomposition of three primary colors generated from multi-dielectric nanostructures are shown in Figure S1. For all periods ranging from 300 to 400 nm, highly monochromatic spectra can be realized owning to suppressed quadrupole modes at shorter wavelength. Figure S1(c, f and i) present the simulated phase distribution for electric dipole and magnetic dipole, respectively. It is clear to see that all three nanostructures are able to cover full 2π space. Besides, there is a slight diffraction effect at wavelength ranging from 400 to 450 nm when the period is set as 400 nm. This is because the metasurface does not meet subwavelength condition as the period becomes close to operation wavelength. In the calculation of multipolar decomposition, we expand the total scattering power into electric dipole (ED), magnetic dipole (MD), electric quadrupole (EQ) and magnetic quadrupole (MQ). In the case of harmonic excitation $\exp(i\omega t)$, the power of scattering cross section can be expressed as

$$\mathrm{I}=\frac{2\omega^4}{2\mathrm{c}^3}|\mathbf{P}|^2+\frac{2\omega^4}{2\mathrm{c}^3}|\mathbf{M}|^2+\frac{\omega^6}{5\mathrm{c}^5}Q_{\alpha\beta}Q_{\alpha\beta}+\frac{\omega^6}{20\mathrm{c}^5}M_{\alpha\beta}M_{\alpha\beta}. \qquad (S1)$$

Here, the four terms represent scattering from ED, MD, EQ and MQ, respectively. In this equation,

ED moment is $\mathbf{P}=\frac{1}{i\omega}\int \mathbf{j}d^3r$,

MD moment is $\mathbf{M}=\frac{1}{2c}\int(\mathbf{r}\times\mathbf{j})d^3r$,

EQ moment is $Q_{\alpha\beta}=\frac{1}{i\omega}\int\left[r_\alpha j_\beta+r_\beta j_\alpha-\frac{2}{3}(\mathbf{r}\cdot\mathbf{j})\right]d^3r$,

MQ moment is $M_{\alpha\beta}=\frac{1}{3c}\int\left[(\mathbf{r}\times\mathbf{j})_\alpha r_\beta+(\mathbf{r}\times\mathbf{j})_\beta r_\alpha\right]d^3r$,

where **j** represent current density and *c* is light speed. [1-2]

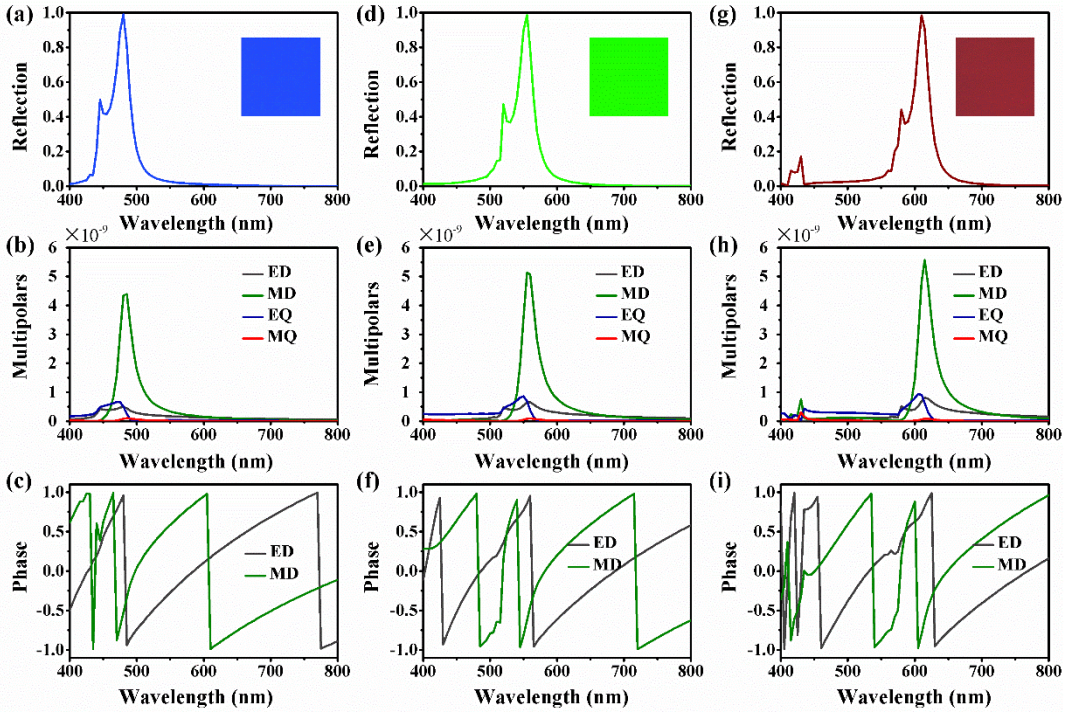

Figure S1: Reflection spectra and multipolar decomposition of three primary colors. (a, d, g) When the gap is fixed at 110 nm, the reflection spectra calculated by COMSOL Multiphysics for nanostructures when the period are 300, 350, and 400 nm, respectively. The insets show corresponding measured colors captured by CCD camera. (b, e, h) Corresponding simulated multipolar decomposition for scattering cross section. (c, f, i) Simulated phase distribution for electric dipole and magnetic dipole, respectively.

S2 Comparison between different anti-reflection designs

We designed two anti-reflection coating methods to demonstrate our design strategy. First, the capping and bottom layers are set as graded-index (GRIN) with index of n_1 and n_3:

$$n_1 = \frac{n_{air} - n_{TiO_2}}{2}\cos\left(\frac{\pi}{\mathrm{H}_1}(z - \mathrm{H}_2 - \mathrm{H}_3) + \pi\right) + \frac{n_{air} + n_{TiO_2}}{2}, \qquad \text{(S2)}$$

$$n_3 = \frac{n_{silica} - n_{TiO_2}}{2} \cos\left(\frac{\pi}{H_3} z\right) + \frac{n_{silica} + n_{TiO_2}}{2}, \quad \text{(S3)}$$

where H_1, H_2 and H_3 respectively represent the thickness of capping layer, spacer layer and bottom layer. Such GRIN distribution makes n_1 smoothly vary from air to TiO_2, and makes n_3 smoothly vary from TiO_2 to the silica substrate (Figure S2a and S2b). Since reflection happens on the boundary of two different media, the GRIN configuration could significantly reduce the reflection. The total thickness of three layers and the thickness of TiO_2 layer are set as 300 nm and 140 nm, respectively, which are the same as those of the dielectric structures in the main text. Compared with the all-TiO_2 nanostructures, the GRIN coating could significantly suppress the multipolar intensity at short working wavelengths, which is one of the key points to increase the saturation of structural colors.

Another anti-reflection design is achieved following the index matching condition (Figure S2c and S2d). We designed the capping layer $n_1 = \sqrt{n_{air} n_{TiO_2}}$ with $H_1 = \lambda_0 / 4n_1(\lambda_0)$, and the bottom layer $n_3 = \sqrt{n_{TiO_2} n_{silica}}$ with $H_3 = \lambda_0 / 4n_3(\lambda_0)$. Here, the optimized wavelength λ_0 is set as 480 nm, where the reflection spectrum shows a peak higher than 0.25 for all-TiO_2 structures. The reflection spectrum also shows a small dip at 480 nm, demonstrating the validity of the design strategy, which can also significantly suppress the multipolar intensity at short working wavelengths for the multi-dielectric nanostructures.

Note that the total thickness of three layers is maintained as 300 nm in all above simulations. From these two different methods we conclude that the anti-reflection design is an efficient strategy to improve the saturation of dielectric structural colors.

In our study, we employed SiO_2 and Si_3N_4 to achieve the index matching condition, and optimized the thickness of the two layers around the theoretical thickness values, which elaborately alters the effective index of each layer and guarantees the index matching condition at short working wavelengths.

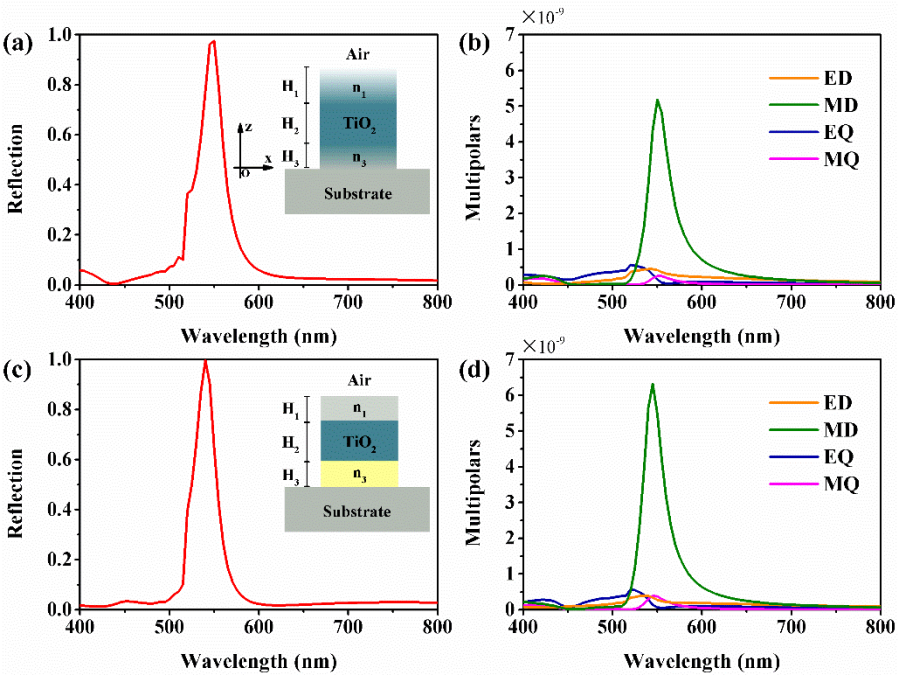

Figure S2. Anti-reflection coating of the dielectric nanostructure. (a, b) GRIN coating of the capping and bottom layer with H_1 = 135 nm, H_2 = 140 nm, H_3 = 25 nm (total thickness of 300 nm). The reflection (a) and multipolar intensity (b) are both significantly suppressed at short wavelengths compared with all-TiO_2 nanostructures. (c, d) Theoretical index matching design of the capping and bottom layer with H_1 = 77 nm, H_2 = 160 nm, H_3 = 63 nm (total thickness of 300 nm). The reflection (c) and multipolar intensity (d) are also significantly suppressed at short wavelengths compared with all-TiO_2 nanostructures.

S3 Influence of different stacked layers

To prove the roles of SiO_2 capping layer and Si_3N_4 layer, simulated reflection spectra and multipolar decomposition for different nanostructures with fixed 200 nm width arranged in 350 nm lattice are presented in Figure S3. In Figure S3a, the reflected efficiency at nonresonant wavelength is invariably high, resulting from the excitation of multipolar modes within all-TiO_2 nanostructures. When putting 100 nm SiO_2 layer on the top of TiO_2 layer as shown in Figure S3e, the reflected efficiency at wavelength from 400 to 500 nm can be slightly suppressed, while at wavelength from 600 nm to 800 nm can be strongly suppressed due to the index matching of SiO_2 layer between TiO_2 layer and air in terms of $\sqrt{n_{TiO_2} n_{air}} \approx n_{SiO_2}$. To further improve the monochromaticity of spectra, we added a 60 nm Si_3N_4 layer under TiO_2 layer, as shown in Figure S3g. The refractive index of Si_3N_4 layer between silica substrate and TiO_2 layer meets the index matching condition $\sqrt{n_{sillca} n_{TiO2}} \approx n_{Si_3N_4}$, resulting in full suppression at visible wavelength from 400 nm to 800 nm. This indicates that more reflected light can be confined in visible wavelength of mono-color, i.e., higher saturation. Hence, multi-dielectric nanostructures consisting of SiO_2 and Si_3N_4 layers as anti-reflection layers can drastically enhance saturation of visible colors.

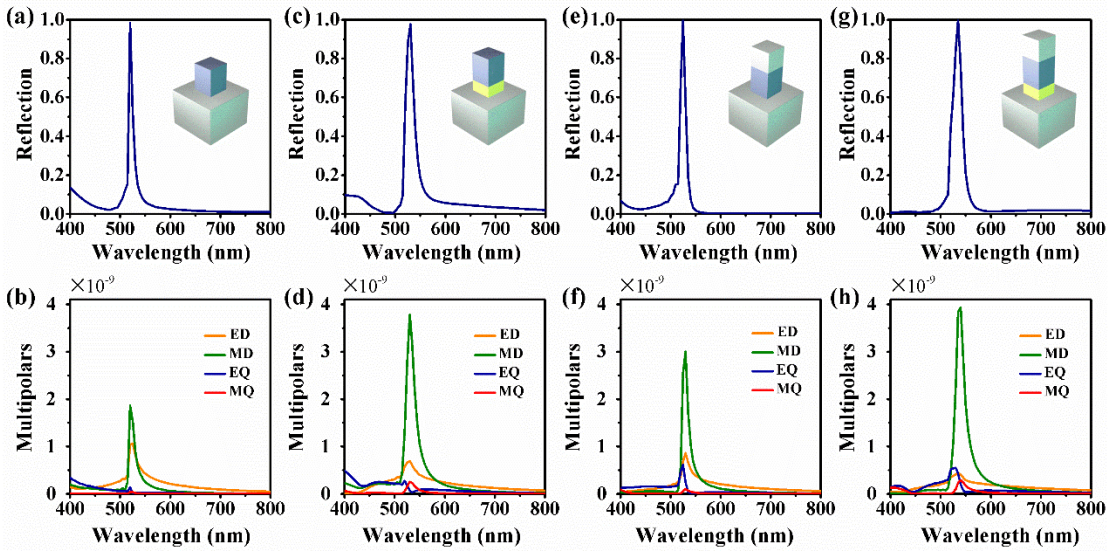

Figure S3. Influence of different dielectric stacked layers. Simulated reflection spectra of nanostructures composed of (a) 140 nm thick TiO_2 nanostructure, (c) 140 nm thick TiO_2 nanostructure with 60 nm Si_3N_4 layer, (e) 140 nm thick TiO_2 nanostructure with 100 nm SiO_2 capping layer, and (g) 140 nm thick TiO_2 nanostructure simultaneously with 100 nm SiO_2 layer and 60 nm Si_3N_4 layer, respectively. Insets show the schematic diagrams of unit cell. (b, d, f and h) Corresponding multipolar decomposition of scattering cross section across the visible waveband.

S4 Deep modulation for higher-order mode by varying index of capping layer and bottom layer

To investigate the role of the capping layer, we simulated the multipolar decomposition of multi-dielectric nanostructures with distinct capping layer in Figure S4a-f. The insets illustrate the unit cell of multi-dielectric nanostructures, where the spacer layer is TiO_2, the bottom layer is Si_3N_4 and the capping layer hold varying indices from 1.1 to 2.1. Since the influence of capping layer with varying indices is more drastic at shorter

wavelength, we enlarge the distribution of EQ mode at wavelength ranging from 400 to 500 nm in Figure S4h. It is clear to see that that EQ mode can be modulated by the refractive index of capping layer. In particular, EQ can be maximally suppressed when the refractive index is fixed at 1.5. That's because the capping layer can be taken as anti-reflection coat when the index matching satisfies the equation of $\sqrt{n_{\mathrm{TiO_2}} n_{air}} = n_{\mathrm{coat}} \approx 1.55$. Hence, we use SiO_2 with 1.46 refractive index as the capping layer.

In this context, all the resonant modes at non-resonant wavelength, in particular EQ mode, can be eliminated at the greatest extent. Accordingly, Figure S4g presents the corresponding reflection spectra at 400-500 nm. The efficiency at nonresonant wavelength can drop to below 1%, which can enhance greatly the monochromaticity of visible spectra.

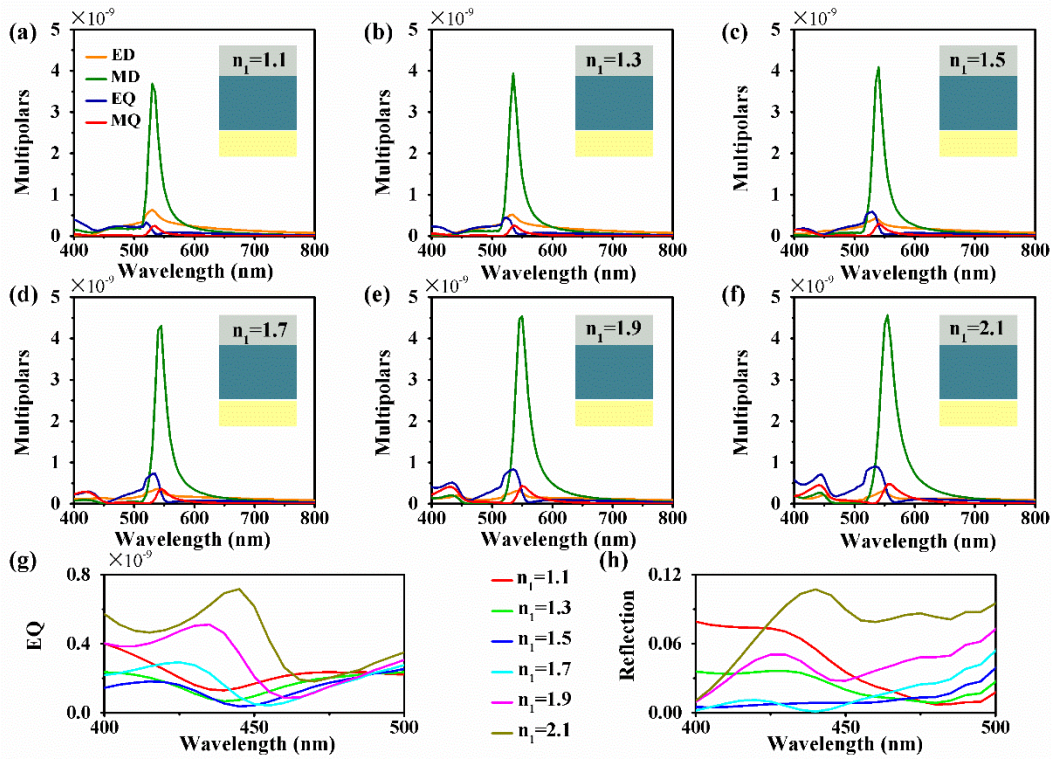

Figure S4: Deep modulation for higher order mode by varying index of capping layer.

(a-f) Calculated multipolar decomposition of scattering cross section when the refractive index of capping layer is (a) 1.1, (b) 1.3, (c) 1.5, (d) 1.7, (e) 1.9, and (f) 2.1, respectively. (g) Magnifying distribution of EQ mode for various refractive indices of capping layer. (h) Reflection spectra at 400 - 500 nm with the refractive indices of capping layer.

To investigate the role of the bottom layer, we simulated the multipolar decomposition of multi-dielectric nanostructures for different refractive indices of Si_3N_4 layer in Figure S5a-f. The refractive index of Si_3N_4 layer varies from 1.4 to 2.4, which corresponds approximately to the variation from silica to TiO_2. The FWHM of reflection spectra gradually increases with the increasing of refractive index of Si_3N_4 layer (Figure S5g). The refractive index of Si_3N_4 layer can approximately meet the index matching condition as an anti-reflection layer between TiO_2 layer and silica at n_3=2.0. In this case, the reflection at short wavelength can be maximally suppressed, and we can get a reflection spectrum with narrow FWHM realizing maximum saturation.

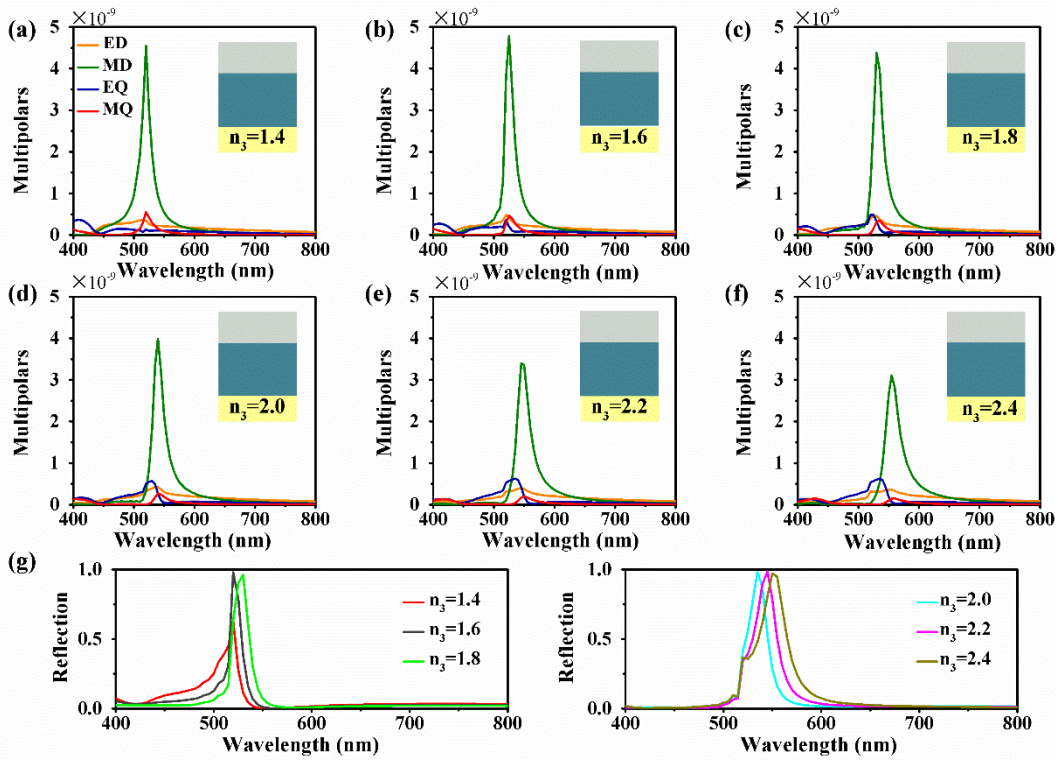

Figure S5. (a-f) Simulated intensity of the multipolar modes for different refractive indices of Si_3N_4 layer with (a) n_3 = 1.4, (b) n_3 =1.6, (c) n_3 = 1.8, (d) n_3 =2.0, (e) n_3 = 2.2, (f) n_3 = 2.4. (g) Reflection spectra for different refractive indices of Si_3N_4 layer.

S5. Angle-dependence properties for multi-dielectric and all-TiO_2 nanostructures

Since the angle-dependent properties are of great importance for display applications, we simulated the angle-dependent performances of the multi-dielectric and all-TiO_2 nanostructures for both *s*-polarization and *p*-polarization states in Figure S6, where the period, width, and total height are 350 nm, 200 nm, and 300 nm, respectively. For the case of *s*-polarization state, the highly saturated structural colors of multi-dielectric nanostructures are nearly independent of incident angle (Figure S6a). The reflection efficiency decreases slightly when the incident angle is varying within 60°, indicating the multi-dielectric nanostructure holds weak angular dependence. However, the angle-

dependent performance of all-TiO_2 nanostructures with the same geometric parameters is relatively sensitive to incident angle compared with that of multi-dielectric nanostructures (Figure S6c). This is because the multi-dielectric nanostructures are an approximation of GRIN media, in which the incident light could more easily couple into the nanostructures. One the other hand, the reflection peak mainly originates from the magnetic mode, which is attributed to the electric component parallel to the top surface of the nanostructures. For *p*-polarization state, the angle-dependent performances of the multi-dielectric and all-TiO_2 nanostructures are sensitively dependent of incident angle (Figure S6b, d). The reason is that the electric component parallel to the top surface decreases when increasing of the incident angle, resulting in red-shift of reflected peak. Overall, the proposed nanostructures hold high angle-insensitivity property under s-polarization state, which is of great significance for displays.

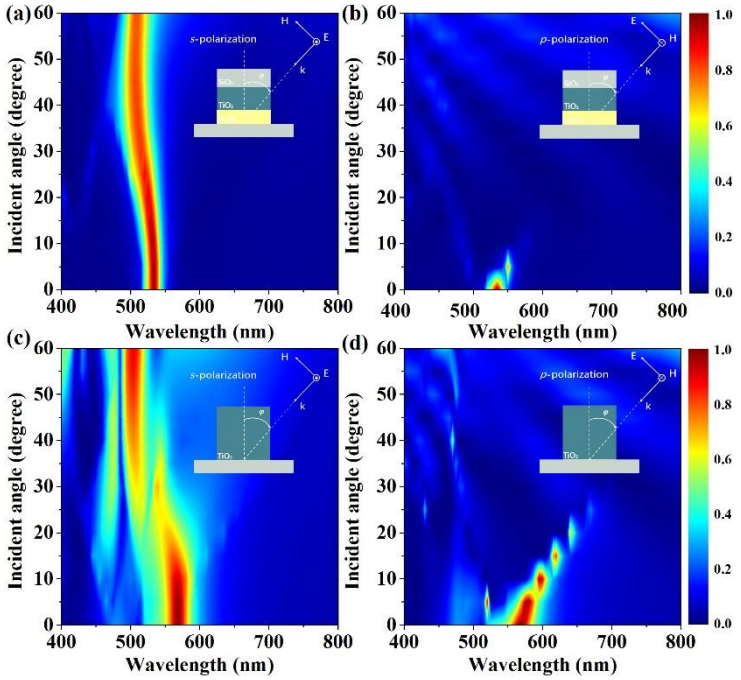

Figure S6. Simulated angular dispersion of the reflection spectra for (a, b) multi-dielectric nanostructures and (c, d) all-TiO_2 nanostructures for both (a, c) *s*- and (b, d) *p*-polarization states.

S6 Area of distinct color standard gamut in 1931 CIE chromaticity diagram

Since 1953, plenty of color standard gamut have been set in 1931 CIE diagram to meet the need of practical applications in various fields. For the past few years, there are four important color gamuts, which are sRGB (standard RGB) in 1996 for monitor, printer and the Internet; Adobe RGB in 1999 for computer displays, high-end camera and imaging applications; DCI-P3 (digital cinema Initiatives) in 2005 for digital movie projection; and Rec. 2020 in 2012 for ultra-high-definition television (UHDTV). To express the color gamut that multi-layer nanostructures generated, we calculated the area of color gamut according to colors' coordinates in CIE diagram. As a result, the area of the CIE color gamut is 0.3357, while the area of the four standard gamut is 0.1117, 0.1520, 0.1507 and 0.2119, respectively. Moreover, the area of the simulated color gamut, consisting of 55 colors from nanostructures with different geometric sizes, is 0.1905, which takes up 57% of CIE color, 171% sRGB, 127% Adobe, 126% DCI-P3 and 90% Rec. 2020 gamut. However, the area of the measured color gamut drops to 0.1422 due to fabrication error, which takes up 128% of sRGB, 95% Adobe RGB, 94% DCI-P3 and 68% Rec.2020 gamut. As far as we know, the current displaying applications with Rec. 2020 gamut is still very rare. Hence, the multi-layer nanostructures in simulation have huge potential to realize Rec. 2020 gamut and be

extensively applied in imaging applications, displays, UHDTV, high-end digital camera and so on.

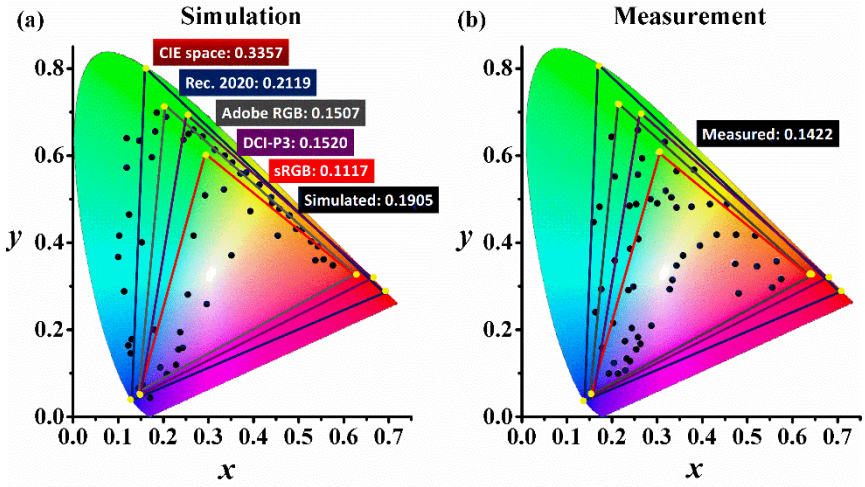

Figure S7: Area of distinct color standards in 1931 CIE chromaticity diagram. (a) Simulated and (b) measured colors gamut.

S7 Measured reflection spectra with varying gap sizes for three primary colors

To study the influence of gap size, Figure S8 shows measured reflection spectra with gap size varying from 110 nm to 190 nm when the period is 300 nm, 350 nm and 390 nm, respectively. It is clearly seen that there is a blue shift for spectra accompanying efficiency drop with the gap size. This is due to smaller interaction space between light and nanostructures at large gap. As illustrated in the insets, however, reduced efficiency and peak broadening make the saturation of colors drop off.

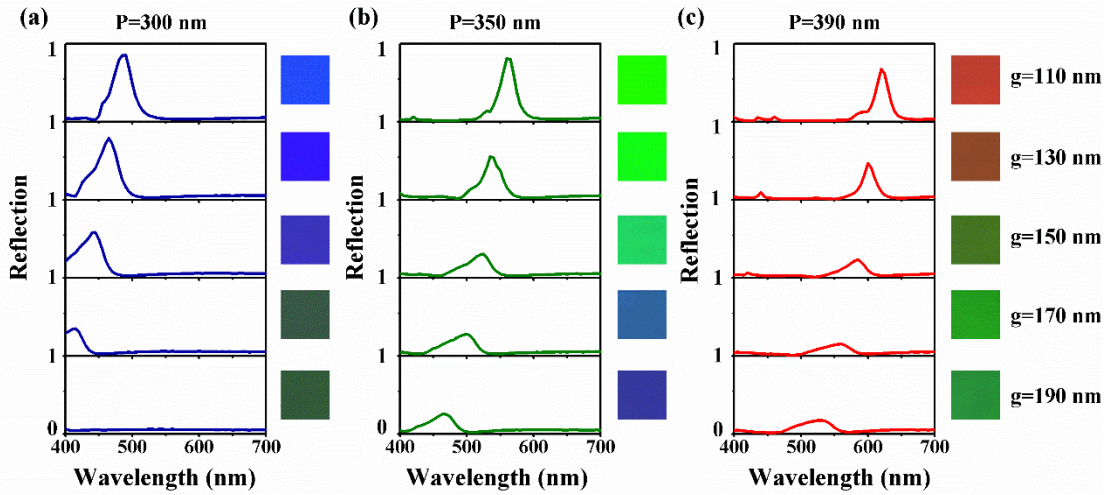

Figure S8: Measured reflection spectra with varying gap sizes for three primary colors. When the period of the multi-dielectric nanostructures is fixed at (a) 300 nm, (b) 350 nm, and (c) 390 nm, the distribution of reflection spectra changes with the gap size at the step of 20 nm in measurement. The insets show the corresponding colors captured by CCD camera.

References

1. Zu, S.; Bao, Y.; Fang, Z. *Nanoscale* **2016**, *8*, 3900-3905.
2. Kaelberer, T.; Fedotov, V. A.; Papasimakis, N.; Tsai, D. P; Zheludev, N. I. *Science* **2010**, *330*, 1510-1512.